

New *s*-process Mechanism in Rapidly-Rotating Massive Pop II Stars

PROJJWAL BANERJEE,^{1, 2} ALEXANDER HEGER,^{3, 4} AND YONG-ZHONG QIAN^{5, 4}

¹ Department of Physics, Indian Institute of Technology Palakkad, Palakkad, Kerala 678557, India

² Department of Astronomy, School of Physics and Astronomy, Shanghai Jiao Tong University, Shanghai 200240, China

³ Monash Centre for Astrophysics, School of Physics and Astronomy, Monash University, Vic 3800, Australia

⁴ Tsung-Dao Lee Institute, Shanghai 200240, China

⁵ School of Physics and Astronomy, University of Minnesota, Minneapolis, Minnesota 55455

(Dated: October 14, 2021)

ABSTRACT

We report a new mechanism for the *s*-process in rotating massive metal-poor stars. Our models show that above a critical rotation speed, such stars evolve in a quasi-chemically-homogeneous fashion, which gives rise to a prolific *s*-process. Rotation-induced mixing results in primary production of ^{13}C , which subsequently makes neutrons via $^{13}\text{C}(\alpha, n)^{16}\text{O}$ during core He burning. Neutron capture can last up to $\sim 10^{13}$ s ($\sim 3 \times 10^5$ yr) with the peak central neutron density ranging from $\sim 10^7$ to 10^8 cm^{-3} . Depending on the rotation speed and the mass loss rate, a strong *s*-process can occur with production of elements up to Bi for progenitors with initial metallicities of $[Z] \lesssim -1.5$. This result suggests that rapidly-rotating massive metal-poor stars are likely the first site for the main *s*-process. We find that these stars can potentially explain the early onset of the *s*-process and some of the carbon-enhanced metal-poor (CEMP-*s* and CEMP-*r/s*) stars with strong enrichment attributed to the *s*-process or a mixture of the *r*-process and the *s*-process.

1. INTRODUCTION

Nearly all of the solar abundances of elements heavier than the Fe group came from the slow (*s*) and rapid (*r*) neutron capture processes, with approximately equal contributions from each. It is well known that the main component of the *s*-process producing elements up to ^{209}Bi is associated with low-mass stars of $\sim 1\text{--}3 M_{\odot}$ and occurs during their final stage of evolution, the asymptotic giant branch (AGB) phase (Straniero et al. 1995; Gallino et al. 1998; Arlandini et al. 1999). In addition, massive stars of $\gtrsim 10 M_{\odot}$, which end their lives in core-collapse supernovae (CCSNe), are traditionally associated with a weak component of the *s*-process producing elements with mass numbers up to $A \sim 90$. This process mostly occurs during core He burning and requires relatively high initial metallicities ($[Z] \gtrsim -1$) (Peters 1968; Couch et al. 1974; Lamb et al. 1977; Raiteri et al. 1991; Rauscher et al. 2002; Pignatari et al. 2010). It was shown, however, that a weak *s*-process can occur even in massive metal-poor stars provided they rotate sufficiently fast initially (Pignatari et al. 2008). Further, a

recent study showed that non-rotating massive metal-poor stars with enhanced initial C abundances can also produce a weak *s*-process (Banerjee et al. 2018b). In both cases, the low-metallicity weak *s*-process primarily produces elements up to $A \sim 90$. Another recent study showed that proton ingestion in convective He shells during the late evolution of non-rotating massive metal-poor stars can lead to a neutron-capture process producing a variety of abundance patterns, including those similar to what is attributed to the main *s*-process (Banerjee et al. 2018a).

In this paper we focus on models of rapidly-rotating massive stars that reach the so-called quasi-chemically-homogeneous (QCH) state following core H burning. In such stars, rotation is fast enough to overcome the composition barrier so that they turn into essentially He stars by the end of core H burning. In these models, stars have very little He left on the surface by the time they reach the pre-collapse stage, and subsequently would produce He-deficient Type Ic SNe (SNe Ic). For this reason, rotating stars that reach the QCH state were studied previously as possible progenitors for broad-line SNe Ic (SNe Ic-BL) associated with long gamma-ray bursts (LGRBs) (Yoon & Langer 2005; Yoon et al. 2006; Woosley & Heger 2006) or superluminous SNe Ic (SLSNe

Ic; [Aguilera-Dena et al. 2018](#)). The primary emphasis of those studies, however, was on the connection with LGRB or SLSN-Ic progenitors rather than on the nucleosynthesis. We find that the same models in fact provide a novel mechanism for a rotation-induced *s*-process in massive metal-poor stars.

Whereas a rotation-induced *s*-process in rapidly-rotating massive metal-poor stars was reported previously, stars in those models do not reach the QCH state and only produce mostly elements up to $A \sim 90$ ([Frischknecht et al. 2012, 2016; Choplin et al. 2018](#)). We note, however, that [Limongi & Chieffi \(2018\)](#) reported an efficient *s*-process in rotating metal-poor star of $\lesssim 20 M_{\odot}$ that do not reach the QCH state. In this case, neutron capture is stronger than the typical weak *s*-process and can easily produce elements up to the second *s*-process peak at Ba ($A \sim 138$). The third *s*-process peak at Pb ($A \sim 208$), however, is produced only in the few models for stars of $\lesssim 15 M_{\odot}$ with $[\text{Fe}/\text{H}] = -2$. In contrast, we find that neutron capture in QCH models is dramatically different and much more efficient, and can easily produce elements up to Pb usually attributed to the main *s*-process.

2. METHODS

We study the evolution and nucleosynthesis of rotating stars of $15 M_{\odot}$ and $25 M_{\odot}$ using the 1D hydrodynamic code KEPLER ([Weaver et al. 1978; Rauscher et al. 2003](#)). We focus on progenitors with an initial metallicity of $[Z] = -3$, corresponding to $[\text{Fe}/\text{H}] \sim -3$ for our adopted composition. The detailed composition is scaled from the solar abundances for Be to Zn and the results of Big Bang nucleosynthesis are used for H to Li. The implementation of rotation including the treatment of transport of angular momentum and mixing is the same as presented in [Heger et al. \(2000\)](#). Two free parameters f_c and f_{μ} control the efficiency of mixing due to rotation by specifying the contribution from this mixing to the diffusion coefficient and the sensitivity of this mixing to composition gradients, respectively. The default values are taken to be $f_c = 1/30$ and $f_{\mu} = 0.05$. These values provide a good fit to the observed enhancement of surface nitrogen abundance for rotating stars of $10\text{--}20 M_{\odot}$ ([Gies & Lambert 1992; Villamariz & Herrero 2005](#)) with initial rotation speed of $\sim 200\text{--}300 \text{ km s}^{-1}$ at solar metallicity ([Heger et al. 2000](#)). The effects of magnetic fields resulting from the Taylor-Spruit dynamo ([Spruit 2002](#)) are also taken into account. In particular, the effect of the magnetic torque on angular momentum transport is included as discussed in detail by [Heger et al. \(2005\)](#).

We explore models with rotation speeds v_{rot} ranging from 20 % to 70 % of the critical breakup speed v_{crit} . This range corresponds to equatorial surface rotation velocities of $\sim 200\text{--}700 \text{ km s}^{-1}$ for the $25 M_{\odot}$ progenitor with $[Z] = -3$ upon reaching the zero-age main sequence. The multi-zone nucleosynthesis is followed from the birth of a star to its death in a CCSN using a large adaptive co-processing network. The network includes isotopes from the proton-drip line to the neutron-drip line for elements up to At (atomic number 85), with a maximum of 4670 isotopes. We use the rates in the detailed list of [Rauscher et al. \(2002\)](#). The CCSN explosion is simulated by driving a piston through the collapsing progenitor with the piston velocity adjusted to obtain the desired explosion energy ([Weaver et al. 1978](#)).

Mass loss is important for the evolution of rapidly-rotating massive metal-poor stars, especially during the Wolf-Rayet (WR) stage. For non-WR evolution, we use the mass loss rate from [Nieuwenhuijzen & de Jager \(1990\)](#). We consider a star to be in the WR stage when its effective surface temperature exceeds 10^4 K and its surface H mass fraction drops below 0.4. For WR stars, we compute two types of models where the mass loss rates are reduced from those of [Hamann et al. \(1995\)](#) by factors of three (M1) and ten (M2), respectively. The former reduction was suggested by [Hamann & Koesterke \(1998\)](#) to account for clumping and the latter was suggested by [Yoon et al. \(2006\)](#) for metal-poor WR stars. We use a scaling law $\propto Z^{0.5}$ to account for the metallicity dependence of the mass loss rate, where Z is taken to be the initial metallicity of the star and does not include any heavy elements produced during its evolution.

3. RESULTS

We find that for v_{rot} above a certain fraction of v_{crit} , stars in all our models reach the QCH state following evolution on the main sequence. This result is consistent with previous studies where similar QCH evolution was found ([Yoon & Langer 2005; Woosley & Heger 2006](#)). Stars in those studies essentially become rigidly rotating He stars with surface H mass fraction of $< 10\%$ by the time He is ignited at the center. Because of the rigid rotation, the density gradient is shallow, with $\gtrsim 95\%$ of the star's mass at densities of $\gtrsim 0.1 \text{ g cm}^{-3}$ and very little mass in a low-density envelope. The minimum initial rotation velocity v_{min} required for the transition to the QCH state depends slightly on the mass, with lower mass progenitors requiring faster rotation. For example, in models with $[Z] = -3$, this transition occurs at 40 % and 30 % of the critical velocity for stars of $15 M_{\odot}$ and $25 M_{\odot}$, respectively.

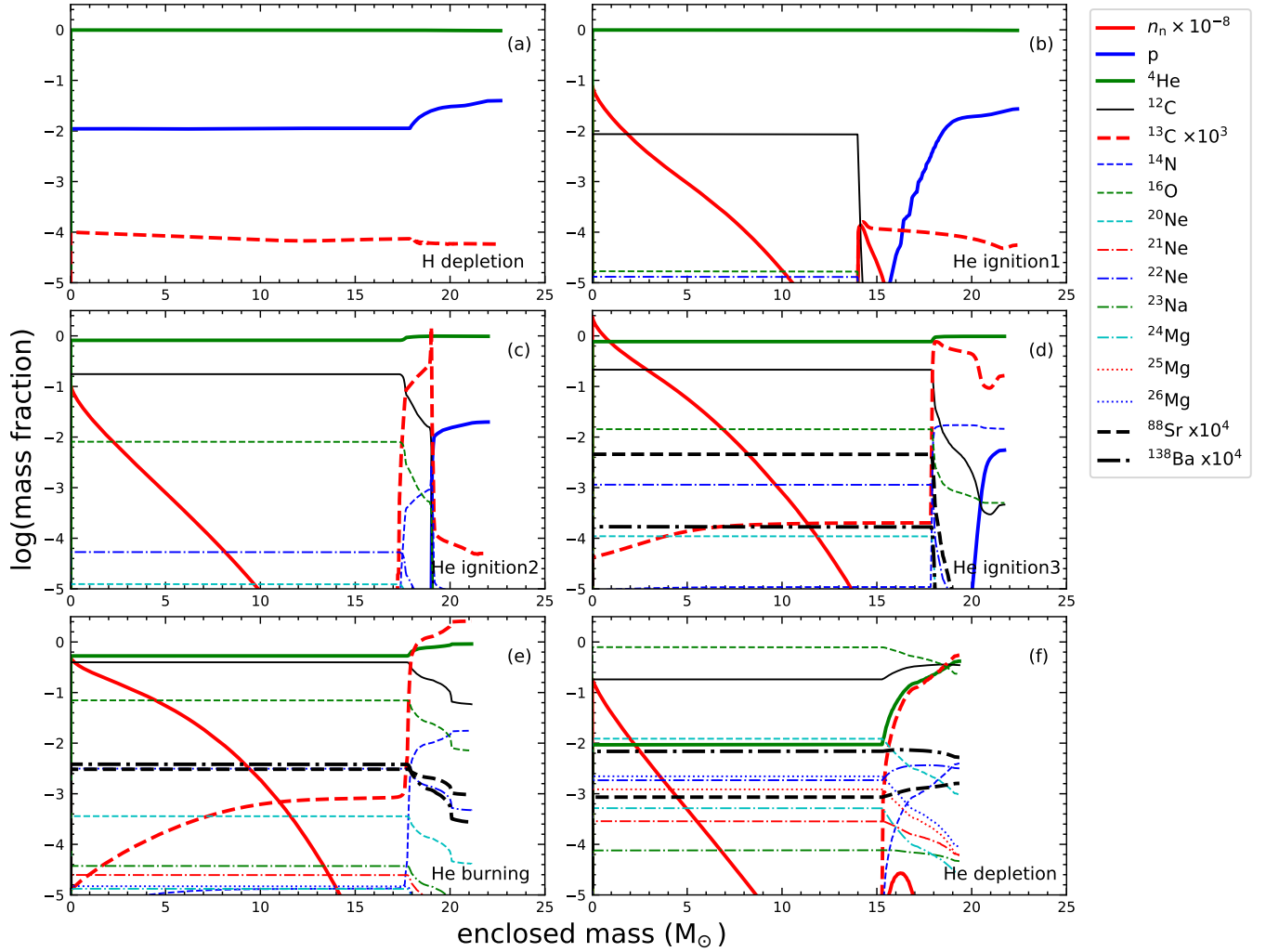


Figure 1. Neutron number abundance (in cm^{-3}) and mass fractions of other light isotopes as functions of mass coordinate at different stages of stellar evolution, from central H depletion (a) to central He depletion (f) for the M1 model of a $25 M_{\odot}$ star with an initial metallicity of $[Z] = -3$ and an initial rotation speed of $v_{\text{rot}} = 0.5 v_{\text{crit}}$. Neutron number abundance is scaled down by a factor of 10^8 . Mass fractions of ^{13}C is scaled up by a factor of 10^3 . Mass fractions of the neutron-capture isotopes ^{88}Sr and ^{138}Ba are scaled up by a factor of 10^4 and shown for reference. (a) H depletion: when the central H mass fraction drops to 1% following core H burning, (b) He ignition1: when the central ^{12}C mass fraction reaches 1%, (c) He ignition2 and (d) He ignition3: intermediate between (b) and (e), (e) He burning: when the central He mass fraction drops to 50%, (f) He depletion: when the central He mass fraction drops to 1%.

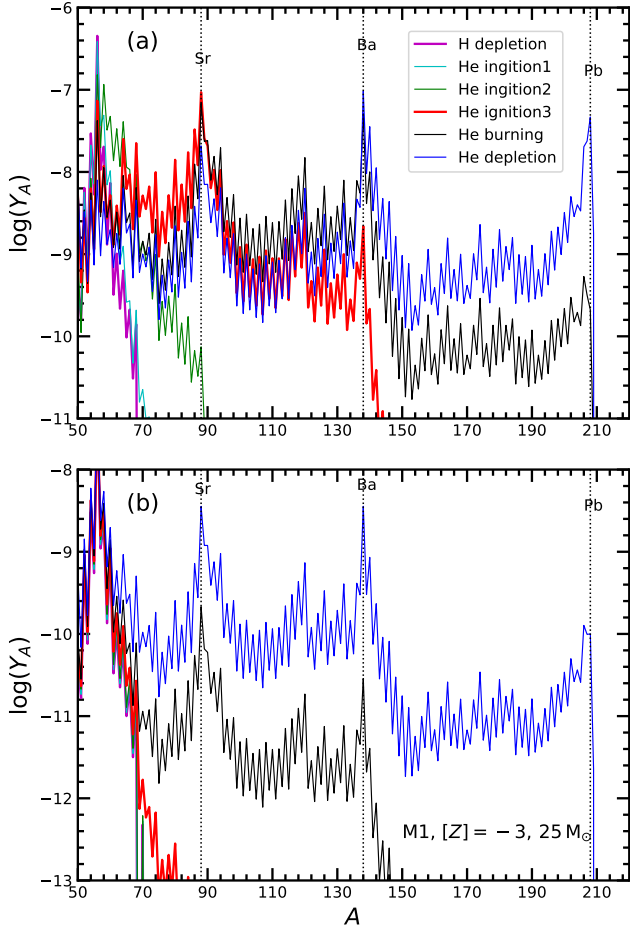


Figure 2. (a) Number yields of heavy isotopes inside the star as functions of mass number corresponding to the evolution stages plotted in Figs. 1a (magenta), 1b (cyan), 1c (green), 1d (red), 1e (black), and 1f (blue). (b) Same as (a) but for the cumulative wind ejecta at the corresponding stages.

3.1. *s*-process in QCH Models

We find that all stars that reach the QCH state undergo the *s*-process. On reaching the QCH state, the star starts to burn He in the center and its core becomes convective. At this stage, although the star is mostly a He star, crucially, it is not completely homogeneous. Specifically, in the outer radiative region of the star, beyond the convective He core, protons are still present, with a typical mass fraction of $\sim 1\text{--}3\%$ (Fig. 1a-c). This turns out to be the key ingredient that enables a subsequent *s*-process to occur. As the size of the convective He core grows, primary ^{12}C is synthesized and quickly becomes abundant, with a mass fraction of ~ 0.2 (Fig. 1c). Due to rotation-induced mixing, some of the ^{12}C is slowly mixed outwards into the radiative region outside the convective core where protons

are available. Because of the QCH evolution, this region has densities of $\sim 10\text{--}30\text{ g cm}^{-3}$ and temperatures of $\sim (7\text{--}8) \times 10^7\text{ K}$ so that the ^{12}C can react efficiently with the protons. The resulting gradual accumulation of ^{13}C can reach mass fractions of up to $\sim 0.1\%$ in this region (Fig. 1c-d). Again due to rotation-induced mixing, some of the ^{13}C is slowly mixed back into the convective He-burning core. Additionally, some of the ^{13}C is slowly ingested as the convective core grows outwards. Once the ^{13}C gets into the convective core, it is transported inward towards hotter regions with a central temperature of $\sim 2 \times 10^8\text{ K}$, where it can react efficiently with the abundant ^4He to produce neutrons via the reaction $^{13}\text{C}(\alpha, n)^{16}\text{O}$. The resulting neutron density is typical of the *s*-process, ranging from $\sim 10^7$ to 10^8 cm^{-3} at the center. The corresponding *s*-process can last the most part of the He-burning phase, which is up to $\sim 10^{13}\text{ s}$ ($\sim 3 \times 10^5\text{ yr}$) for a 25 M_\odot star. The time evolution of the *s*-process yield pattern is shown in Fig. 2 for the M1 Model of a 25 M_\odot star with an initial metallicity of $[Z] = -3$ and an initial rotation speed of $v_{\text{tot}} = 0.5 v_{\text{crit}}$. Pre-CCSN yields of Sr, Ba, Eu, and Pb are given in Table 1 for a number of models.

In the same layers where ^{13}C is synthesized, a substantial amount of primary ^{14}N is also produced through the CNO cycle (Figs. 1c-f). The ^{14}N is then mixed into the convective core similarly to ^{13}C and acts as a potent neutron poison. In addition, during the later stages of core He burning, primarily-produced ^{16}O becomes sufficiently abundant with a mass fraction of $\gtrsim 0.1$ and starts to be an important neutron poison. Near the end of He burning, other primary poisons, such as ^{20}Ne and $^{24,25,26}\text{Mg}$, also begin to act as significant neutron sinks (Figs. 1e-f). Thus, primary neutron poisons become increasingly important to counter neutron production by the primary ^{13}C during the later stages of core He burning. Nevertheless, neutron capture continues until He is completely exhausted at the center, resulting in an overall strong *s*-process with production of elements up to Bi.

It is well known that most of the ^{14}N mixed into the convective He-burning core is efficiently converted into ^{22}Ne via $^{14}\text{N}(\alpha, \gamma)^{18}\text{F}(e^+ \nu_e)^{18}\text{O}(\alpha, \gamma)^{22}\text{Ne}$. ^{22}Ne can produce neutrons via $^{22}\text{Ne}(\alpha, n)^{25}\text{Mg}$ and is in fact the main neutron source for the rotation-induced *s*-process at low metallicities found by Pignatari et al. (2008) and Frischknecht et al. (2012, 2016). In our QCH models, ^{22}Ne also becomes the dominant neutron source during the very late stages of He burning (Fig. 1f). Their contribution to the overall strong *s*-process, however, is negligible compared to that of ^{13}C .

Table 1. Pre-CCSN yields (in M_{\odot}) of Sr, Ba, Eu, and Pb for selected models reaching the QCH state. Here $X(Y) \equiv X \times 10^Y$.

Model	Sr	Ba	Eu	Pb
M1, $[Z] = -3, 0.3 v_{\text{crit}}, 25 M_{\odot}$	1.76(-6)	8.11(-10)	1.21(-13)	2.88(-15)
Wind	6.67(-11)	1.30(-17)	1.92(-27)	3.85(-37)
M1, $[Z] = -3, 0.4 v_{\text{crit}}, 25 M_{\odot}$	1.93(-6)	1.45(-5)	2.80(-8)	5.98(-6)
Wind	3.01(-7)	2.74(-7)	1.46(-10)	5.48(-9)
M1, $[Z] = -3, 0.5 v_{\text{crit}}, 25 M_{\odot}$	1.30(-6)	1.05(-5)	2.86(-8)	1.94(-5)
Wind	3.62(-7)	6.83(-7)	6.45(-10)	8.95(-8)
M2, $[Z] = -3, 0.3 v_{\text{crit}}, 25 M_{\odot}$	1.81(-6)	9.98(-6)	2.30(-8)	2.65(-5)
Wind	1.05(-10)	1.68(-21)	1.94(-24)	3.11(-22)
M2, $[Z] = -3, 0.4 v_{\text{crit}}, 25 M_{\odot}$	1.14(-6)	5.63(-6)	1.70(-8)	5.40(-5)
Wind	1.02(-7)	4.74(-7)	1.05(-9)	8.74(-7)
M2, $[Z] = -3, 0.5 v_{\text{crit}}, 25 M_{\odot}$	6.70(-7)	1.90(-6)	4.44(-9)	7.61(-5)
Wind	6.41(-8)	2.40(-7)	5.65(-10)	4.84(-6)
M1, $[Z] = -3, 0.4 v_{\text{crit}}, 15 M_{\odot}$	4.40(-6)	1.73(-6)	1.10(-9)	1.69(-8)
Wind	4.52(-9)	1.17(-11)	3.46(-16)	3.38(-16)
M1, $[Z] = -3, 0.5 v_{\text{crit}}, 15 M_{\odot}$	1.49(-6)	8.03(-6)	1.19(-8)	3.32(-6)
Wind	1.56(-7)	6.21(-8)	2.86(-11)	1.27(-9)
M2, $[Z] = -3, 0.4 v_{\text{crit}}, 15 M_{\odot}$	1.38(-6)	7.49(-6)	1.37(-8)	8.06(-6)
Wind	1.64(-8)	1.31(-8)	6.82(-12)	3.86(-10)
M2, $[Z] = -3, 0.5 v_{\text{crit}}, 15 M_{\odot}$	1.08(-6)	5.07(-6)	1.34(-8)	2.15(-5)
Wind	7.88(-8)	2.66(-7)	4.63(-10)	2.35(-7)

3.2. Effects of Mass Loss and Rotation

For the same stellar mass, initial metallicity, and initial rotation speed, neutron capture is more efficient in the M2 model with a lower WR mass loss rate, primarily because less mass loss leads to less loss of angular momentum. For a $25 M_{\odot}$ progenitor with $[Z] = -3$, we find that rotation is faster in the M2 model by $\sim 30\%$ than that in the M1 model during core He burning. Faster rotation induces more mixing, thereby facilitating a more efficient *s*-process. The effect of mass loss on the *s*-process efficiency is particularly evident for slower initial rotation speeds near the v_{min} required to reach the QCH state. For example, for a $25 M_{\odot}$ progenitor with $v_{\text{rot}} = 0.3 v_{\text{crit}}$, the *s*-process flow only reaches Sr ($A \sim 90$) in the M1 model. In contrast, the *s*-process flow easily reaches Bi ($A \sim 209$) in the M2 model (Figs. 3).

Following the above discussion, we expect that for the same stellar mass, initial metallicity, and mass loss, faster initial rotation would give rise to more efficient neutron capture, and hence, a stronger *s*-process. This trend, however, is valid only up to a certain rotation speed. Then the *s*-process efficiency saturates or even starts to decrease slightly. For example, for the M1 models of a $25 M_{\odot}$ progenitor with $[Z] = -3$, the *s*-process efficiency, as indicated by the production of Pb relative to Ba, is marginally less for $v_{\text{rot}} = 0.7 v_{\text{crit}}$ than for

$v_{\text{rot}} = 0.6 v_{\text{crit}}$, whereas the efficiency is almost identical for the corresponding M2 models (Fig. 3-4). The saturation, or slight decrease, of the *s*-process efficiency is caused by the competition between production of the neutron poison, ^{14}N , and that of the neutron source, ^{13}C . The former starts to slowly dominate the latter at sufficiently high rotation speed. Nevertheless, the *s*-process is still very efficient for $v_{\text{rot}} = 0.7 v_{\text{crit}}$, the fastest speed considered in our study.

For a $25 M_{\odot}$ progenitor with $[Z] = -3$, we find that the *s*-process can robustly produce Bi in the M2 model once the initial rotation is fast enough to reach the QCH state, i.e., $v_{\text{rot}} = 0.3 v_{\text{crit}}$. For $v_{\text{rot}} > 0.3 v_{\text{crit}}$, a very efficient *s*-process in the M2 model leads to overproduction of Pb relative to Ba and Sr (Fig. 3b). Clearly, faster initial rotation can compensate for more severe loss of angular momentum due to more mass loss in the M1 model. For a $25 M_{\odot}$ progenitor, we find that an initial rotation speed of $v_{\text{rot}} \gtrsim 0.4 v_{\text{crit}}$ is required to produce Bi in the M1 model (Figs. 3a).

As shown in Figs. 3 and 4, the effects of mass loss and rotation on the *s*-process are evident in the yield patterns both inside the star and for the wind ejecta.

3.3. Effects of Initial Metallicity

As discussed above, mass loss leads to angular momentum loss, which affects rotation-induced mixing responsible for producing the primary ^{13}C neutron source. Be-

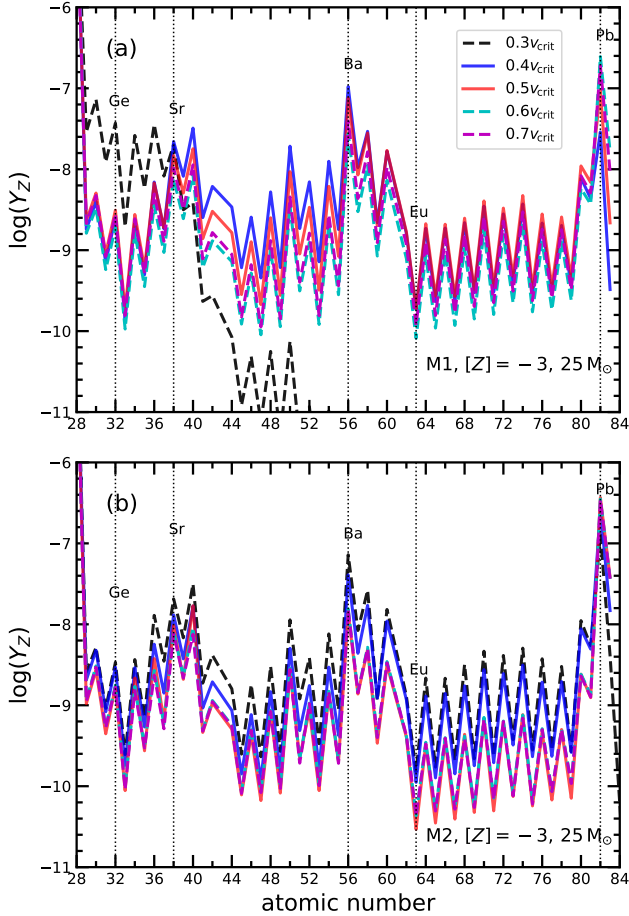


Figure 3. (a) Number yields of heavy elements inside the star as functions of atomic number for the M1 models of a $25 M_{\odot}$ star with an initial metallicity of $[Z] = -3$ and with varying initial rotation speeds of 30 % (black), 40 % (blue), 50 % (red), 60 % (cyan), and 70 % (purple)

of v_{crit} . (b) Same as (a) but for the M2 models.

cause the mass loss rate increases with the initial metallicity Z , the s -process efficiency depends on Z . In addition, for progenitors with $[Z] \gtrsim -2$, neutron poisons inherited from the birth material start to become important. Consequently, the efficiency of the s -process is adversely affected in higher-metallicity progenitors, with the effect being particularly strong in the M1 models with more mass loss. For example, for the M1 models of a $25 M_{\odot}$ progenitor with an initial rotation speed of $v_{\text{rot}} = 0.5 v_{\text{crit}}$, rotation during core He burning is a factor of ~ 2.6 slower for $[Z] = -2$ than that for $[Z] = -3$, which accounts for the negligible s -processing in the $[Z] = -2$ model (Fig. 5a). Similarly, for the M2 models, rotation is slower by a factor of ~ 1.6 for $[Z] = -2$ than that for $[Z] = -3$. Rotation in the M2 model for $[Z] = -2$, however, is still $\sim 10\%$ faster than that in the M1 model for $[Z] = -3$. Therefore, a sub-

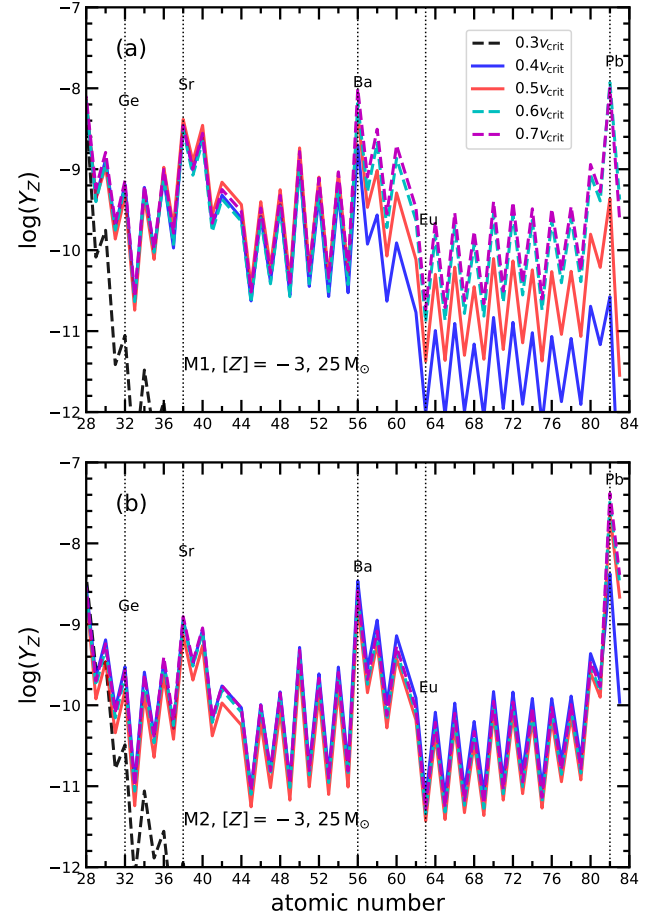


Figure 4. (a) Same as Fig. 3a, but for the wind ejecta. (b) Same as Fig. 3b, but for the wind ejecta.

stantial s -process occurs in the M2 model for $[Z] = -2$, although it is less efficient, i.e., has a lower Pb/Ba ratio, than the s -process in the M2 model for $[Z] = -3$ (the higher absolute yields for $[Z] = -2$ are due to the more abundant seeds from the higher initial metallicity, Fig. 5b). When the metallicity reaches $[Z] = -1.5$, the main s -process is no longer possible, but substantial production of heavy elements up to $A \sim 90$ can still occur through the weak s -process in the M2 models (Fig. 5).

3.4. Composition of Wind Ejecta

Because of the QCH evolution, stars in our models reach the WR stage well before H is depleted at the center. Thus, significant mass loss through winds starts long before the occurrence of the s -process during core He burning and continues until the end of the star's life. The composition of the wind ejecta changes over time in terms of both the heavy s -process and the light elements. This change depends on the slow rotation-induced mixing of material from the convective core towards the surface and on the mass loss that affects the

efficiency of this mixing. As a result of this mixing, a gradient in composition is produced between the core and the surface. In particular, as the *s*-process proceeds to heavier elements in the core, the *s*-process composition on the surface always lags behind that in the core and has a lower enrichment. For example, by the time the *s*-process in the core has reached Pb, the surface has only been enriched approximately up to Ba (Fig. 2). Thus, the *s*-process composition of the wind ejecta may not reach the heaviest elements produced in the core. For the same reason, by the end of the star's life, the net composition of all the wind ejecta is also less enriched in the *s*-process elements compared to the core (Table 1). Nevertheless, the net wind composition can easily reach Bi with substantial enrichment of the heavy *s*-process elements for the M2 models (Fig. 4). In addition to the heavy elements, the wind ejecta is also naturally enriched in CNO from core He burning.

3.5. Evolution Beyond Core He Depletion

Although the *s*-process is essentially over by the end of core He burning, some additional neutron capture can take place during the later stages when the star contracts to burn O at the center. During those stages, the C/O shell still has some He left with a mass fraction of $\gtrsim 10\%$. Due to the overall contraction of the star, the temperature there rises to $\sim 4 \times 10^8$ K with typical densities of $\sim 10^3$ g cm $^{-3}$ so that He can burn convectively. Whereas ^{13}C has already been burned away by then, abundant primary ^{22}Ne with a mass fraction of $\gtrsim 10^{-3}$ in the C/O shell produces neutrons via $^{22}\text{Ne}(\alpha, n)^{25}\text{Mg}$, with the neutron density reaching up to $n_n \sim 10^{11}$ cm $^{-3}$ at the base of the shell. The associated neutron capture can change the abundances of the elements between the *s*-process peaks and turn the earlier *s*-process pattern in the C/O shell into an *r/s*-like pattern, i.e., a pattern in between *s*- and *r*-patterns that is usually similar to what is attributed to the intermediate (*i*) neutron-capture process (Cowan & Rose 1977). For reference, we note that the solar *r*- and *s*-process patterns are characterized by $[\text{Ba/Eu}]_r \sim -0.8$ and $[\text{Ba/Eu}]_s \sim 1.6$, respectively. In this paper we refer to patterns with $[\text{Ba/Eu}] \gtrsim 1$ as *s*-like and $[\text{Ba/Eu}] < 1$ as *r/s*-like.

C burning in the convective O/Ne shell during the later stages of evolution also gives rise to high neutron densities of up to $n_n \sim 5 \times 10^{12}$ cm $^{-3}$ at the base of the shell, where the neutron source is again the primary ^{22}Ne . Initially, neutron capture at higher n_n at the base of the shell is able to dominate that at much lower n_n in the outer part of the shell, thereby modifying the abundance pattern in the shell into an *r/s*-like one. As ^{22}Ne gets depleted, however, neutron density at the base

of the O/Ne shell drops, so that neutron capture at lower n_n in the outer colder part of the shell brings the pattern back to an *s*-like one. In contrast, due to the overall low n_n , neutron capture in the outer part of the He burning C/O shell is never able to dominate that at the base of the shell so that the *r/s*-like pattern is preserved until core collapse. We find that $[\text{Ba/Eu}]$ as low as ~ 0.65 can be preserved in the He burning C/O shell.

Although neutron capture after core He depletion can modify the abundance pattern between the peaks as described above, it makes a negligible contribution to the net *s*-process as the abundance peaks at Sr, Ba, and Pb remain practically unchanged. This result comes about simply because very low neutron exposure is provided during the limited time ($\lesssim 10^8$ s) available before core collapse. Nevertheless, the higher neutron densities reached during this time can change the *s*-process pattern into an *r/s*-like one. By the end of the star's life, however, only the *r/s*-like pattern in the C/O shell can survive. Nevertheless, it is remarkable that we can obtain an *r/s*-like pattern by modifying an existing *s*-process pattern at neutron densities of $\sim 10^{11}$ – 10^{12} cm $^{-3}$, which are much lower than those typically required for an *i*-process to occur, i.e., $\gtrsim 10^{14}$ cm $^{-3}$.

With regard to the structure, the QCH evolution turns the star into a He star, where the He core spans almost the entire star and is comparable to those of non-rotating stars that are $\gtrsim 2$ – 3 times more massive. Following core He depletion and subsequent stages of central C, O, and Si burning in these large He cores, the pre-collapse structure of the $15 M_\odot$ and $25 M_\odot$ models corresponds to that of non-rotating stars of $\gtrsim 40 M_\odot$ with relatively high compactness. A compactness parameter ξ_M (O'Connor & Ott 2011) is defined as

$$\xi_M = \frac{M/M_\odot}{R(M)/1000 \text{ km}}, \quad (1)$$

where R_M is the radius enclosing a certain baryonic mass M . The value of ξ_M just before core collapse is considered a good indicator for the likelihood of a successful neutrino-driven SN explosion, with a low likelihood for ξ_M above a critical value (O'Connor & Ott 2011; Sukhbold & Woosley 2014). For the usual choice of $M = 2.5 M_\odot$, the QCH stars at the pre-SN stage have $\xi_M \sim 0.33$ – 0.45 . These values are too large for the standard neutrino-driven explosion to work (Ertl et al. 2016; Müller et al. 2016; Sukhbold et al. 2016). Therefore, these stars are likely to produce a weak SN or might even fail to explode unless their rapid rotation facilitates non-neutrino-driven explosion such as in magnetorotational or jet-driven SNe associated with LGRBs (see Woosley & Heger 2012 and Nagataki 2018 for reviews)

or in SLSNe powered by the spin-down of magnetars (Woosley 2010; Kasen & Bildsten 2010).

Regardless of the details of the explosion, the pre-SN winds from these rotating stars ensure that a substantial amount of the *s*-process material is always ejected into the interstellar medium (ISM). Any material ejected during the explosion will add to the wind ejecta. Provided that an explosion can be launched, we find that a large amount of material might be ejected even in the presence of severe fallback. For example, with our simple piston prescription for the artificially-induced explosion, the outer ~ 6 (7) M_{\odot} of the stellar core is ejected in addition to the wind ejecta of ~ 6 (3) M_{\odot} from a $25 M_{\odot}$ star with $[Z] = -3$ in the M1 (M2) models for a typical explosion energy of 1.2×10^{51} ergs. Interestingly, the ejecta from the explosion includes the C/O shell with the *r/s*-like pattern for the heavy elements. We note, however, that long-term 3D simulations such as those by Chan et al. (2018) are required to estimate reliably the amount of material ejected during the explosion.

4. DEPENDENCE ON TREATMENT OF MIXING

In order to test the sensitivity of the *s*-process in QCH models to the particular choice of mixing parameters, we performed another set of calculations for the same f_c but with a twice larger value of $f_{\mu} = 0.10$. For $10-20 M_{\odot}$ stars with typical initial rotational speed of $\sim 200 \text{ km s}^{-1}$ at solar metallicity, such a choice of parameters gives a slightly lower surface nitrogen enhancement than observed (Heger et al. 2000). For both, the M1 and M2 models of a $25 M_{\odot}$ star with initial metallicity of $[Z] = -3$, the *s*-process yields obtained with $f_{\mu} = 0.10$ are almost identical to those for the default value of $f_{\mu} = 0.05$ (Fig. 6). This result suggests that the *s*-process studied here is not very sensitive to reasonable choice of parameters for rotation-induced mixing.

As is typical of 1D codes, all our default calculations used smoothing of gradients in treating rotation-induced instabilities. We also repeated the calculations for the M1 and M2 models of a $25 M_{\odot}$ star with initial metallicity of $[Z] = -3$ without smoothing. The resulting *s*-process is almost unchanged except for some differences in the Pb abundance when compared to the default calculations (Fig. 7). This indicates that smoothing does not significantly affect the *s*-process in QCH models.

5. DISCUSSION AND CONCLUSIONS

Rapidly-rotating massive metal-poor stars reaching the QCH state can be a natural site for the main *s*-process. Without becoming fully chemically homogeneous He stars, these QCH stars have a relatively minor amount of H present in the outer parts, which ultimately gives rise to the ^{13}C neutron source through

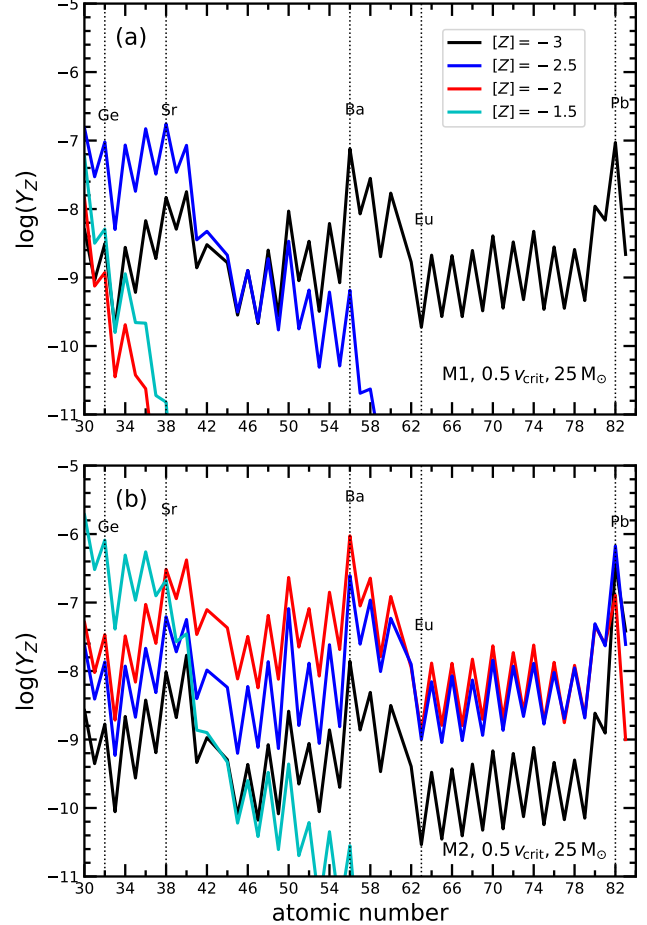


Figure 5. (a) Number yields of heavy elements inside the star as functions of atomic number for the M1 models of a $25 M_{\odot}$ star with an initial rotation speed of $0.5 v_{\text{crit}}$ and with varying initial metallicities of $[Z] = -3$ (black), -2.5 (blue), -2.0 (red), and -1.5 (cyan). (b) Same as (a) but for the M2 models.

rotation-induced mixing. Although neutron production in these stars is independent of the initial metallicity, the efficiency of the *s*-process decreases with increasing metallicity. Higher metallicity leads to more mass loss, which in turn slows down the rotation, thereby decreasing the efficiency of rotation-induced mixing critical to the *s*-process. A strong *s*-process is possible only in QCH models of massive stars with initial metallicities of $[Z] \lesssim -1.5$.

The *s*-process in rapidly-rotating massive metal-poor stars discussed here would have direct implications for the chemical evolution of heavy elements in the early Galaxy as revealed by observations of elemental abundances in low-mass ($\lesssim 0.8 M_{\odot}$) very metal-poor (VMP) stars with $[\text{Fe}/\text{H}] \lesssim -2$. Such VMP stars are thought to have formed within ~ 1 Gyr after the Big Bang and their surface abundances are considered to directly re-

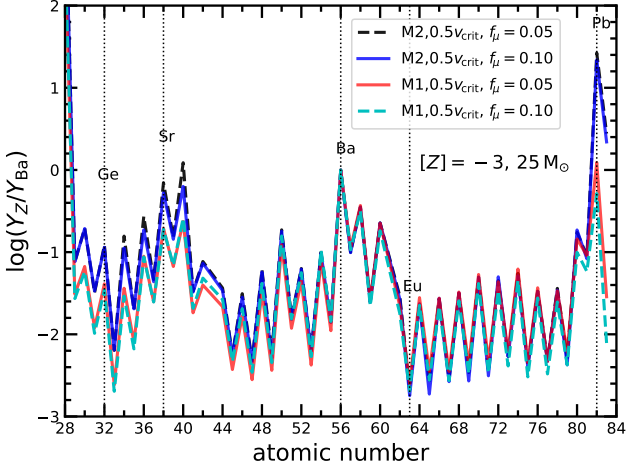


Figure 6. Number yields of heavy elements relative to Ba inside the star as functions of atomic number for the M1 and M2 models of a $25 M_{\odot}$ star with an initial rotation speed of $0.5 v_{\text{crit}}$ and $[Z] = -3$ for the default value of $f_{\mu} = 0.05$ compared to the corresponding models with $f_{\mu} = 0.10$.

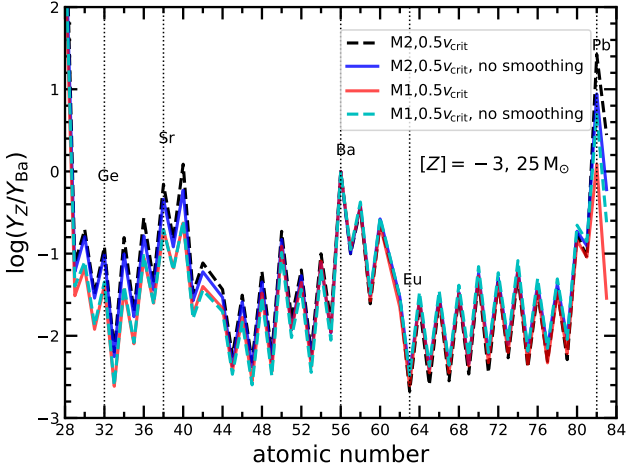


Figure 7. Number yields of heavy elements relative to Ba inside the star as functions of atomic number for the M1 and M2 models of a $25 M_{\odot}$ star with an initial rotation speed of $0.5 v_{\text{crit}}$ and $[Z] = -3$ using the default smoothing for rotation-induced mixing compared to the corresponding models without smoothing.

flect the composition of the ISM from which they were formed. Because the main *s*-process is usually associated with long-lived low-mass stars that could not have contributed to the chemical enrichment during the first ~ 1 Gyr, it is commonly assumed that the heavy elements with $A \gtrsim 120$ observed in VMP stars must have originated exclusively from the *r*-process associated with early short-lived massive stars. Yet deviations from the expected *r*-process pattern, which is characterized by $[\text{Ba/Eu}]_{\text{r}} = -0.8$, were observed in VMP stars with

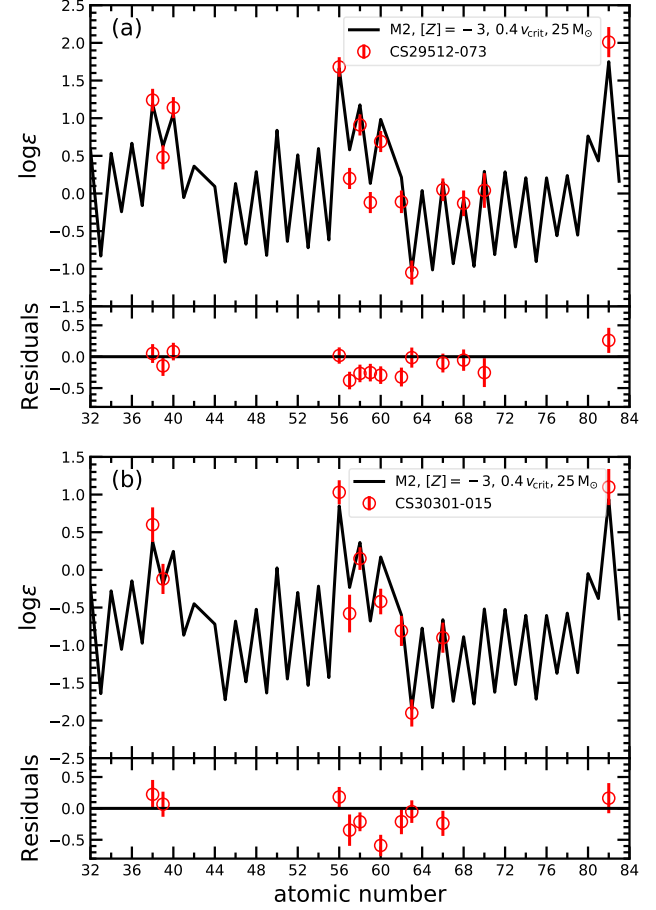


Figure 8. (a) Heavy-element abundances from the wind ejecta in the M2 model of a $25 M_{\odot}$ star with an initial metallicity of $[Z] = -3$ and an initial rotation speed of $0.4 v_{\text{crit}}$ compared to data for the CEMP-*s* star CS29512-073 (Roederer et al. 2014). A dilution mass of $100 M_{\odot}$ is used. (b) Same as (a), but for the CEMP-*s* star CS30301-015 (Aoki et al. 2002a) with a dilution mass of $650 M_{\odot}$.

$[\text{Fe/H}]$ as low as ~ -3.5 (Suda et al. 2008; Simmerer et al. 2004). Further, there exists a sub-class of VMP stars called the carbon-enhanced metal-poor (CEMP) stars (Beers & Christlieb 2005), which are highly enriched in C with $\log \epsilon(\text{C}) \sim 8.0 \pm 0.4$ and $[\text{C/Fe}] > 0.7$ (Spite et al. 2013; Bonifacio et al. 2015; Hansen et al. 2015; Yoon et al. 2016). Most of the CEMP stars are the so-called CEMP-*s* stars, which are also enriched in heavy elements with $[\text{Ba/Fe}] > 1$ and have abundance patterns exhibiting $[\text{Ba/Eu}] > 0.5$, similar to what is expected from the main *s*-process. The *s*-process discussed here can explain at least some of the above observations.

Clearly, our models of rapidly-rotating massive metal-poor stars provide an early source for the main *s*-process that naturally accounts for the early onset of this process as revealed by the abundance patterns of some VMP

stars. In addition, our models can explain at least some CEMP-s stars. Whereas most CEMP-s stars are in binaries (Lucatello et al. 2005), observations suggest that $\sim 10\text{--}30\%$ of them could be single stars (Hansen et al. 2016). If a rapidly-rotating massive metal-poor star had a low-mass binary companion, transfer of the wind material ejected by the massive star onto the surface of the companion would have provided high enrichment of C and the heavy *s*-process elements to the latter. It is possible that the binary would have survived the subsequent evolution and explosion of the massive star, especially if the star collapsed directly into a black hole or the explosion imparted little kick to the black hole left behind. In this scenario, some binary companions of CEMP-s stars would be black holes of $\sim 10 M_{\odot}$ instead of white dwarfs. It is also likely, however, that the binary would have been disrupted. In this case, the low-mass star with its surface already polluted would be observed as a single CEMP-s star today. Of course, single CEMP-s stars could also have been formed directly from the ISM enriched by the winds of rapidly-rotating massive metal-poor stars. In any case, the heavy elements in the wind ejecta can provide good fits to the observed *s*-process patterns. Figure 8 shows example fits to the data on two CEMP-s stars using the wind ejecta from the M2 model of a $25 M_{\odot}$ star with $[Z] = -3$ and $v_{\text{rot}} = 0.4 v_{\text{crit}}$.

A popular model for explaining the high C and *s*-process enrichment in CEMP-s stars involves surface pollution due to mass transfer from a binary companion during its AGB phase (see e.g., Bisterzo et al. 2011). Although this model can successfully explain the abundance patterns in many CEMP-s stars, it has difficulty fitting the patterns in other such stars (Bisterzo et al. 2012; Abate et al. 2015). As it naturally predicts that all CEMP-s stars should be accompanied by white dwarfs left behind by their former AGB companions, it is also in apparent conflict with the existence of single CEMP-s stars. As discussed above, the *s*-process in rapidly-rotating massive metal-poor stars can account for at least some CEMP-s stars, including those in single configuration. Therefore, this explanation is complementary to the popular model for CEMP-s stars.

CEMP stars also include the so-called CEMP-*r/s* stars. These stars have similar properties to CEMP-s stars, i.e., high enrichment in C and heavy elements, but have abundance patterns that appear to be a mixture of those from the *r*-process and the *s*-process. The origin of the heavy elements in CEMP-*r/s* stars is still unresolved, although a number of models have been proposed (Cohen et al. 2003; Barbuy et al. 2005; Jonsell et al. 2006; Dardelet et al. 2014). Recent studies showed that the *i*-process might be the most likely explanation

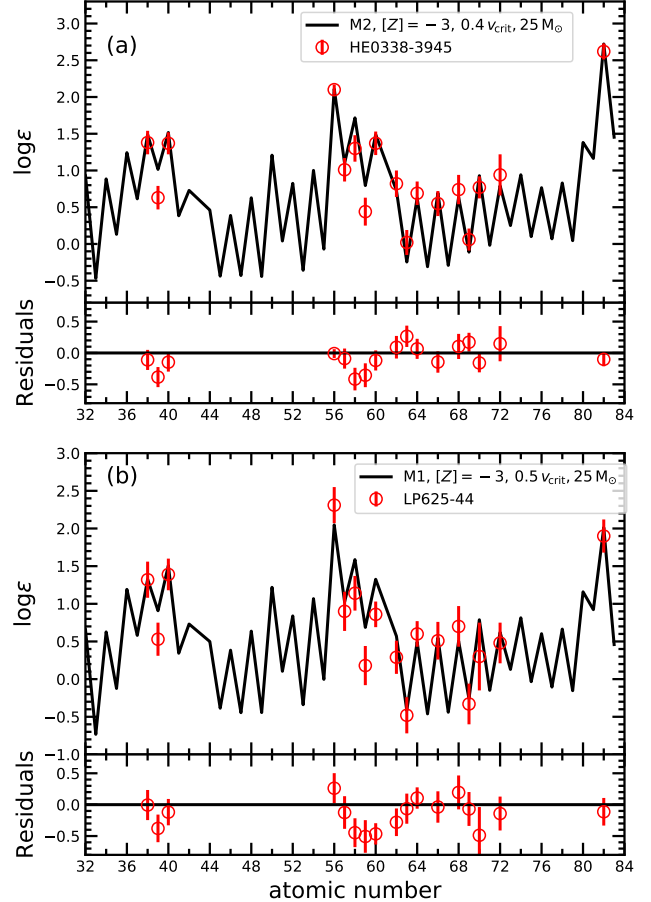


Figure 9. (a) Heavy-element abundances from the mixture of the outer stellar and wind ejecta in the M2 model of a $25 M_{\odot}$ star with an initial metallicity of $[Z] = -3$ and an initial rotation speed of $0.4 v_{\text{crit}}$ compared to data for the CEMP-*r/s* star HE0338-3945 (Jonsell et al. 2006). A dilution mass of $180 M_{\odot}$ is used. (b) Same as (a), but for the M1 model with an initial rotation speed of $0.5 v_{\text{crit}}$ compared to data for the CEMP-*r/s* star LP625-44 (Aoki et al. 2002b) with a dilution mass of $180 M_{\odot}$.

(Lugardo et al. 2012). This process can naturally produce the abundance patterns in most CEMP-*r/s* stars (Hampel et al. 2016). Consequently, these stars are now also referred to as CEMP-*i* stars. The proposed sites for the *i*-process include low to intermediate mass stars of $\lesssim 8 M_{\odot}$ (Fujimoto et al. 2000; Campbell et al. 2010; Herwig et al. 2011; Jones et al. 2016), massive stars of $\sim 20\text{--}30 M_{\odot}$ (Banerjee et al. 2018a) or more (Clarkson et al. 2018), and accreting white dwarfs (Denissenkov et al. 2017, 2019). In our models, during core O burning, the outer part of the star, specifically the C/O shell, experiences additional neutron capture that eventually modifies the abundance pattern from *s*-like to *r/s*-like. If this material is ejected in addition to the wind ejecta, the resulting abundance pattern can fit some of the

CEMP-*r/s* stars. Figure 9 shows example fits to the data on two CEMP-*r/s* stars using the mixture of the outer stellar and wind ejecta from a $25 M_{\odot}$ star with $[Z] = -3$ for the M2 model (with $v_{\text{rot}} = 0.4 v_{\text{crit}}$) and M1 model (with $v_{\text{rot}} = 0.5 v_{\text{crit}}$), respectively. For the model shown in Fig. 9a, adding the outer stellar core material to the wind changes [Ba/Eu] from 1.03 to 0.69 while for the model in Fig. 9b, [Ba/Eu] changes from 1.65 to 0.88. Surprisingly, we can explain these two CEMP-*r/s* stars with our models despite our neutron densities are much lower than those required for the *i*-process ($\gtrsim 10^{14} \text{ cm}^{-3}$). As discussed in § 3.5, an *r/s*-like pattern is obtained in our models by modifying an earlier *s*-process pattern at neutron densities of $\sim 10^{11}$ – 10^{12} cm^{-3} . For this reason, we do not refer to CEMP-*r/s* stars as CEMP-*i* stars here. The lowest [Ba/Eu] that can be achieved in the outer stellar core, however, is ~ 0.65 , hence CEMP-*r/s* with $[\text{Ba/Eu}] < 0.65$ cannot be explained by the rotating models discussed here. The *i*-process might be required to explain such stars, making them bona fide CEMP-*i* stars.

Another site for neutron capture in non-rotating massive metal-poor stars (Banerjee et al. 2018a) can also help explain the early onset of the *s*-process, CEMP-*s* stars, and CEMP-*r/s* stars. This site relies on proton ingestion into convective He shells to provide neutrons and can produce a variety of abundance patterns including those similar to what are attributed to the main *s*-process and the *i*-process. Whereas 3D models are required to calculate reliably the ingestion and transport of protons, only parametric 1D studies were performed by Banerjee et al. (2018a) to explore the associated nucleosynthesis. Ideally, 3D models should also be used to follow the evolution of rotating stars, especially rotation-induced mixing that is critical to neutron production in the 1D QCH models presented here. We are well aware of the limitations of our 1D models, but note that they are guided by observations and have been used to study topics other than nucleosynthesis.

This work covers a relatively small grid of progenitor mass, initial metallicity, and initial rotation speed. The limited set of models studied, however, is sufficient to elucidate the mechanism and main features of the *s*-process in rapidly-rotating massive metal-poor stars, which is the main goal of this paper. We plan to cal-

culate a larger set of models to obtain a more comprehensive picture. In particular, the dependence on the two free parameters f_c and f_{μ} , which control the efficiency of rotation-induced mixing, needs to be explored further. We stress, however, that their values adopted in this work are identical to those used in earlier studies and were not tuned to obtain the *s*-process of interest here. In this sense, the *s*-process is likely robust in rapidly-rotating massive metal-poor stars reaching the QCH state. Nevertheless, whether a star can reach the QCH state may depend on the physics model and numerical implementation. Whereas the QCH state in rotating massive stars was reported by Yoon & Langer (2005), Yoon et al. (2006), and Woosley & Heger (2006), other studies did not find this state (Pignatari et al. 2008; Frischknecht et al. 2012, 2016; Cholpin et al. 2018). The latter make different choices with regard to use of magnetic fields and dynamo, use different smoothing algorithms, etc. Although the treatment of mixing in all these models was calibrated to match the observed surface ^{14}N enhancement at core hydrogen depletion for massive stars with $v_{\text{rot}} \sim 200$ – 300 km s^{-1} at solar metallicity, they give different results for the evolution beyond core hydrogen depletion and for faster rotation speeds that are not constrained by observations. Clearly, these differences are due to those in the use and implementation of rotation-induced mixing in 1D stellar evolution codes. Future code comparison studies are required to shed light on this issue. Finally, as shown here, mass loss impacts the efficiency of the *s*-process in QCH models by slowing down rotation. In view of the uncertainties in mass loss from WR stars, especially at very low metallicities, the effects of different mass loss prescriptions also need to be explored further. In addition, the synthesis of CNO and other light elements in QCH models will be explored in the near future.

This work was supported in part by the National Natural Science Foundation of China [11533006 (SJTU), 11655002 (TDLI)], the US Department of Energy [DE-FG02-87ER40328 (UM)], and the Science and Technology Commission of Shanghai Municipality [16DZ2260200 (TDLI)].

Software: KEPLER (Weaver et al. 1978; Rauscher et al. 2003; Heger et al. 2005).

REFERENCES

Abate, C., Pols, O. R., Izzard, R. G., & Karakas, A. I.

2015, *A&A*, 581, A22

Aguilera-Dena, D. R., Langer, N., Moriya, T. J., &

Schootemeijer, A. 2018, *ApJ*, 858, 115

Aoki, W., Ryan, S. G., Norris, J. E., et al. 2002a, *ApJ*, 580, 1149

Aoki, W., Ando, H., Honda, S., et al. 2002b, *PASJ*, 54, 427

Arlandini, C., Käppeler, F., Wissak, K., et al. 1999, *ApJ*, 525, 886

Banerjee, P., Qian, Y.-Z., & Heger, A. 2018a, *ApJ*, 865, 120

—. 2018b, *MNRAS*, 480, 4963

Barbuy, B., Spite, M., Spite, F., et al. 2005, *A&A*, 429, 1031

Beers, T. C., & Christlieb, N. 2005, *ARA&A*, 43, 531

Bisterzo, S., Gallino, R., Straniero, O., Cristallo, S., & Käppeler, F. 2011, *Mon. Not. R. Astron. Soc.*, 418, 284

—. 2012, *Mon. Not. R. Astron. Soc.*, 422, 849

Bonifacio, P., Caffau, E., Spite, M., et al. 2015, *A&A*, 579, A28

Campbell, S. W., Lugaro, M., & Karakas, A. I. 2010, *A&A*, 522, L6

Chan, C., Müller, B., Heger, A., Pakmor, R., & Springel, V. 2018, *ApJ*, 852, L19

Choplin, A., Hirschi, R., Meynet, G., et al. 2018, *A&A*, 618, A133

Clarkson, O., Herwig, F., & Pignatari, M. 2018, *MNRAS*, 474, L37

Cohen, J. G., Christlieb, N., Qian, Y.-Z., & Wasserburg, G. J. 2003, *ApJ*, 588, 1082

Couch, R. G., Schmiedekamp, A. B., & Arnett, W. D. 1974, *ApJ*, 190, 95

Cowan, J. J., & Rose, W. K. 1977, *ApJ*, 212, 149

Dardelet, L., Ritter, C., Prado, P., et al. 2014, in XIII Nuclei in the Cosmos (NIC XIII), 145

Denissenkov, P. A., Herwig, F., Battino, U., et al. 2017, *ApJL*, 834, L10

Denissenkov, P. A., Herwig, F., Woodward, P., et al. 2019, *MNRAS*, 1865

Ertl, T., Janka, H. T., Woosley, S. E., Sukhbold, T., & Ugliano, M. 2016, *ApJ*, 818, 124

Frischknecht, U., Hirschi, R., & Thielemann, F.-K. 2012, *A&A*, 538, L2

Frischknecht, U., Hirschi, R., Pignatari, M., et al. 2016, *MNRAS*, 456, 1803

Fujimoto, M. Y., Ikeda, Y., & Iben, Jr., I. 2000, *ApJL*, 529, L25

Gallino, R., Arlandini, C., Busso, M., et al. 1998, *ApJ*, 497, 388

Gies, D. R., & Lambert, D. L. 1992, *ApJ*, 387, 673

Hamann, W.-R., & Koesterke, L. 1998, *A&A*, 335, 1003

Hamann, W.-R., Koesterke, L., & Wessolowski, U. 1995, *A&A*, 299, 151

Hampel, M., Stancliffe, R. J., Lugaro, M., & Meyer, B. S. 2016, *ApJ*, 831, 171

Hansen, T., Hansen, C. J., Christlieb, N., et al. 2015, *ApJ*, 807, 173

Hansen, T. T., Andersen, J., Nordström, B., et al. 2016, *A&A*, 588, A3

Heger, A., Langer, N., & Woosley, S. E. 2000, *ApJ*, 528, 368

Heger, A., Woosley, S. E., & Spruit, H. C. 2005, *ApJ*, 626, 350

Herwig, F., Pignatari, M., Woodward, P. R., et al. 2011, *ApJ*, 727, 89

Jones, S., Ritter, C., Herwig, F., et al. 2016, *Mon. Not. R. Astron. Soc.*, arXiv:1510.07417

Jonsell, K., Barklem, P. S., Gustafsson, B., et al. 2006, *A&A*, 451, 651

Kasen, D., & Bildsten, L. 2010, *ApJ*, 717, 245

Lamb, S. A., Howard, W. M., Truran, J. W., & Iben, Jr., I. 1977, *ApJ*, 217, 213

Limongi, M., & Chieffi, A. 2018, *ApJS*, 237, 13

Lucatello, S., Tsangarides, S., Beers, T. C., et al. 2005, *ApJ*, 625, 825

Lugaro, M., Karakas, A. I., Stancliffe, R. J., & Rijs, C. 2012, *ApJ*, 747, 2

Müller, B., Heger, A., Liptai, D., & Cameron, J. B. 2016, *MNRAS*, 460, 742

Nagataki, S. 2018, *Reports on Progress in Physics*, 81, 026901

Nieuwenhuijzen, H., & de Jager, C. 1990, *A&A*, 231, 134

O'Connor, E., & Ott, C. D. 2011, *ApJ*, 730, 70

Peters, J. G. 1968, *ApJ*, 154, 225

Pignatari, M., Gallino, R., Heil, M., et al. 2010, *ApJ*, 710, 1557

Pignatari, M., Gallino, R., Meynet, G., et al. 2008, *ApJL*, 687, L95

Raiteri, C. M., Busso, M., Picchio, G., & Gallino, R. 1991, *ApJ*, 371, 665

Rauscher, T., Heger, A., Hoffman, R. D., & Woosley, S. E. 2002, *ApJ*, 576, 323

—. 2003, *Nucl. Phys. A*, 718, 463

Roederer, I. U., Preston, G. W., Thompson, I. B., et al. 2014, *Astron. J.*, 147, 136

Simmerer, J., Sneden, C., Cowan, J. J., et al. 2004, *ApJ*, 617, 1091

Spite, M., Caffau, E., Bonifacio, P., et al. 2013, *A&A*, 552, A107

Spruit, H. C. 2002, *A&A*, 381, 923

Straniero, O., Gallino, R., Busso, M., et al. 1995, *ApJ*, 440, L85

Suda, T., Katsuta, Y., Yamada, S., et al. 2008, *Publ. Astron. Soc. Jpn.*, 60, 1159

Sukhbold, T., Ertl, T., Woosley, S. E., Brown, J. M., & Janka, H. T. 2016, *ApJ*, 821, 38

Sukhbold, T., & Woosley, S. E. 2014, [ApJ](#), 783, 10

Villamariz, M. R., & Herrero, A. 2005, [A&A](#), 442, 263

Weaver, T. A., Zimmerman, G. B., & Woosley, S. E. 1978, [ApJ](#), 225, 1021

Woosley, S. E. 2010, [ApJ](#), 719, L204

Woosley, S. E., & Heger, A. 2006, [ApJ](#), 637, 914

—. 2012, [ApJ](#), 752, 32

Yoon, J., Beers, T. C., Placco, V. M., et al. 2016, [ApJ](#), 833, 20

Yoon, S.-C., & Langer, N. 2005, [A&A](#), 443, 643

Yoon, S.-C., Langer, N., & Norman, C. 2006, [A&A](#), 460, 199